

Two-Dimensional Phosphorus-Doped Carbon Nanosheets with Tunable Porosity for Oxygen Reactions in Zinc-Air Batteries

Wen Lei,^{†,‡} Ya-Ping Deng,[‡] Gaoran Li,[‡] Zachary P. Cano,[‡] Xiaolei Wang,[‡] Dan Luo,[‡] Yangshuai Liu,[‡] Deli Wang,^{*,†} and Zhongwei Chen^{*,‡}

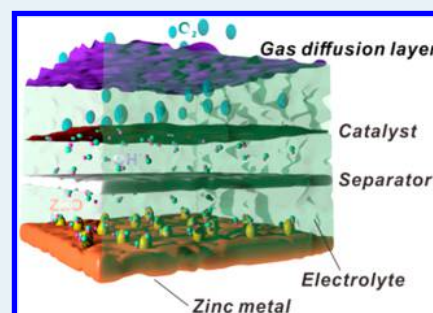
[†]Key laboratory of Material Chemistry for Energy Conversion and Storage (Huazhong University of Science and Technology), Ministry of Education, Hubei Key Laboratory of Material Chemistry and Service Failure, School of Chemistry and Chemical Engineering, Huazhong University of Science and Technology, Wuhan 430074, PR China

[‡]Department of Chemical Engineering, Waterloo Institute for Nanotechnology, Waterloo Institute for Sustainable Energy, University of Waterloo, Waterloo, Ontario N2L 3G1, Canada

Supporting Information

ABSTRACT: Large-sized two-dimensional phosphorus-doped carbon nanosheets (2D-PPCN) with tunable porosity were synthesized via a multifunctional templating method. A single inexpensive solid precursor, phosphorus pentoxide, is combined with common saccharides in a stepwise multiple templating process for 2D construction, phosphorus doping, and regulated micro-/mesopore creation. This reliable 2D porous carbon production technique can potentially be utilized in a variety of energy storage and conversion fields. The effects of different porous structures on the electrocatalytic activity of 2D-PPCN based electrocatalysts are specifically investigated in this work. The interconnected open-pore system and high specific surface area result in a high catalytic efficiency for both the oxygen reduction reaction (ORR) and oxygen evolution reaction (OER). When integrated into an air-breathing cathode for rechargeable Zn-air batteries, the best-performing 2D-PPCN demonstrates better cell performance than a noble metal benchmark catalyst and a higher durability with over 1000 charge–discharge cycles.

KEYWORDS: two-dimensional carbon, porous structure, phosphorus doping, zinc-air batteries



1. INTRODUCTION

The birth of graphene in 2004 triggered great research interest in two-dimensional (2D) materials due to their advantages in frontiers including condensed matter physics, quantum electrodynamics, and materials science, as well as the energy storage and conversion fields.¹ Particularly, 2D materials beyond graphene represented by a series of transition metal oxides,² sulfides,³ and carbides,⁴ as well as various metal-free graphene analogues, such as carbon sheets,⁵ carbon nitride,⁶ silicone,⁷ and phosphorene,⁸ have shown potential in the development of clean, sustainable, and efficient energy technologies. Their structural anisotropy and surface characteristics combined with their intrinsic properties endow these 2D materials with promising mechanical, chemical, and electric merits in fulfilling the requirements of emerging electrochemical technologies.

Among the aforementioned 2D materials, 2D porous carbon materials are rising as a competitive participant in the energy storage and conversion fields. Distinct from the smooth facets and overlapping tendency of graphene, which leads to decreased active surface area and impeded interlayer transportation, 2D porous carbon delivers high porosity with significantly improved mass transfer and enriched active centers.⁹ Beyond that, the aromatic p-conjugated framework and anisotropic planar geometry also ensure excellent electronic conductivity.¹⁰ These virtues render 2D porous carbon

attractive for technologies such as batteries,¹¹ electrocatalysis¹² and electrochemical surface engineering.¹³ Especially, in the electrocatalysis field, the 2D porous carbon materials play an important role as both catalyst and support.¹⁴ However, despite the recent progress of applicable precursors and the persistent optimization of the structural building process, the electrochemical performances of the reported metal-free pure carbon based catalysts are still inferior to that of commercial Pt/C.^{11b} It has been demonstrated that heteroatom doping (e.g., N, B, P, S, etc.) within the porous carbon framework is an effective approach to tuning electronic properties or/and conductivity, which endows them with more favorable electrocatalytic properties.¹⁵

Unfortunately, the state-of-art synthesis of 2D porous carbon generally relies on graphene based assembling/templating, oriented CVD growth, specific biomass conversion, and postactivations, which not only involves complex procedures and rigorous conditions but also lacks the ability to tune porosity to meet the requirements for specific electrochemical applications. When it comes to heteroatom doping, the synthetic procedures become even more complicated.¹⁶

Received: August 13, 2017

Revised: January 29, 2018

Published: February 5, 2018

Therefore, in the absence of scalable and well-controlled methods of production, 2D porous carbon materials cannot achieve their full potential in energy conversion and storage applications.

To address this challenge, we reported a convenient procedure for producing large-size 2D phosphorus-doped porous carbon nanosheets (2D-PPCN) with highly tunable porosity. Inspired by the well-known dehydration and carbonization of saccharides induced by concentrated sulfuric acid,¹⁷ we endeavored to exploit the similar properties of P₂O₅ as a novel carbonizing agent. P₂O₅ is shown to facilitate a series of structural evolutions beyond mere carbonization, including stepwise templating for 2D molding and controllable pore-forming. This leads to the construction of 2D porous carbon rather than the familiar foam-like morphology obtained from sulfuric acid based synthesis. The simplicity of employing two starting materials and a three-step heating procedure, both of which can be optimized for desired porosity and low cost, is attractive to large-scale producers of 2D porous carbon materials.

The demonstrated ability to adjust the porosity and surface area within the 2D-PPCN is further used to investigate the relationships between its structural features and electrocatalytic activity. The porous 2D carbon construction strategy reported in this work is also proved to allow great flexibility by using various carbon precursors. As a representative illustration of its performance, 2D-PPCN was employed as a bifunctional catalyst for both ORR and OER in a rechargeable Zn-air battery. The obtained battery achieved outstanding cyclability over 1000 cycles, surpassing the coupling of commercial Pt/C and Ir/C catalysts, thus supporting the application prospects of 2D-PPCN in electrochemical applications.

2. EXPERIMENTAL SECTION

2.1. Synthesis of 2D Phosphorus-Doped Porous Carbon Nanosheets (2D-PPCN). In a typical procedure, 2.0 g of glucose and 1.0 g of phosphorus pentoxide were ground uniformly for 15 min in a glovebox. The mixture of powder was then sealed into a Teflon-lined stainless steel autoclave (with an internal argon atmosphere) and transferred into an oven, which was heated to 200 °C and kept for 6 h. Afterward, foam-like black product was obtained, which was then put into a tube furnace and annealed at 450 °C under argon gas for 1 h with a ramp rate of 3 °C min⁻¹. The furnace was then heated to 900 °C at a ramp rate of 5 °C min⁻¹, and kept for 3 h. During this period, some red substance appeared on the inner wall of the tube (when the temperature reached about 800 °C). Finally, the black precipitate was collected by filtration, washed two times with deionized water, and dried in a vacuum oven at 80 °C. The same approach was then used to synthesize 2D-PPCNs by using fructose, sucrose, starch, cellulose, and agar as the raw materials. Further, to verify the tunable porosity of 2D-PPCN, control experiments toward synthesis of 2D-PPCN were conducted by varying the amount of P₂O₅ to 1.0 g, 2.0 g, 4.0 g, and 6.0 g (The mass of glucose in the experiment was kept unchanged at 2.0 g). The obtained products were denoted as 2D-PPCN-2/1, 2D-PPCN-2/2, 2D-PPCN-2/4, and 2D-PPCN-2/6, respectively.

2.2. Materials Characterization. X-ray diffraction (XRD) patterns were collected on a Rigaku Miniflex 600 X-ray diffractometer with the 2θ degree in the range of 10° to 80°. The morphology and structure of the samples were analyzed with a JEM-2010F transmission electron microscope and a

Bruker Innova atomic force microscope. X-ray photoelectron spectroscopy (XPS) spectra were collected on an Axis Ultra. Raman spectrometry was performed with a DXR Raman microscope with a frequency diode laser at 532 nm; 2D Raman mapping signals were collected within an area of 300 μm × 200 μm on a SiO₂/Si substrate. The color gradients represent the intensity of the D band, G-band, and 2D band, which are obtained at the same position on the Raman spectrum. Brunauer–Emmett–Teller (BET) analysis was performed to clarify the porosity and pore volume of the developed materials. Specific surface area (*S*_{BET}) was obtained using the BET equation, total pore volume (*V*_{total}) was estimated at a relative pressure of 0.98, micropore volume (*V*_{micro}, determined from the subtraction of mesopore volume from total pore volume) and mesopore volume (*V*_{meso}) were determined from the nonlocal density functional theory (NLDFT) model. Considering there were few macrospores in the synthesized samples, the *V*_{meso} was determined from the subtraction of *V*_{micro} from *V*_{total}.

2.3. Electrochemical Measurements. Electrocatalytic activity measurements were performed in a three-electrode configuration with a Biologic VSP 300. A glassy carbon (GC) disk electrode (5 mm in diameter) served as the working electrode, and a carbon rod (99.999%, Strem Chemicals) was used as the counter electrode. The catalyst suspension was prepared by dispersing 10 mg of catalyst in 1 mL of ethanol under sonication for 30 min to form a homogeneous dispersion. The catalyst suspension was then pipetted using a micropipette onto the GC surface. 0.1 M KOH was used as the electrolyte. After pumping for 30 min, the O₂ bubble rate is then controlled to 60 mL min⁻¹ by a rotameter. The potential was recorded with reference to a saturated calomel electrode (SCE) and was then converted to the reversible hydrogen electrode (RHE) according to the Nernst equation (*E*_{RHE} = *E*_{SCE} + 0.059 × pH + 0.241). The kinetic current (*I*_k) can be calculated using the Koutecky–Levich equation which is expressed by 1/*I* = 1/*I*_k + 1/*I*_d, where *I* is the measured current and *I*_d the diffusion limited current. The *I*_d term can be obtained from the Levich equation: *I*_d = 0.62*nFAD*^{2/3}*v*^{-1/6}*ω*^{1/2}*C*_{O₂}, where *n* is the number of electrons transferred; *F* is Faraday's constant (96,485 C mol⁻¹); *A* is the area of the electrode (0.196 cm²); *D* is the diffusion coefficient of O₂ in 0.1 M KOH solution (1.9 × 10⁻⁵ cm² s⁻¹); *v* is the kinematic viscosity of the electrolyte (1.00 × 10⁻² cm² s⁻¹); *ω* is the angular frequency of rotation, *ω* = 2π*f*/60, *f* is the RDE rotation rate in r.p.m., and *C*_{O₂} is the concentration of molecular oxygen in 0.1 M KOH solution (1.2 × 10⁻⁶ mol cm⁻³).

2.4. Preparation of Air Electrode for Zinc-Air Batteries. 2D-PPCN was dispersed in ethanol and drop-cast loaded on carbon paper (Toray carbon paper TGP-H-120, FuelCellStore) as the air cathode. The mass loading was about 1.0 mg cm⁻². After drying overnight in an oven at 60 °C, the prepared air electrode was paired with a polished Zn foil in 6.0 M KOH with 0.2 M zinc acetate electrolyte. For comparison, a mixture of Pt/C and Ir/C with a mass ratio of 1:1 was also prepared and tested in the same condition. All the Zn-air batteries were tested under ambient atmosphere on a LAND CT2001A multichannel battery testing system.

3. RESULTS AND DISCUSSION

3.1. Formation Mechanism of 2D-PPCN. The formation mechanism of 2D-PPCN is illustrated in Scheme 1. The 2D

Scheme 1. Schematic Illustration of the Synthesis Route for 2D-PPCN

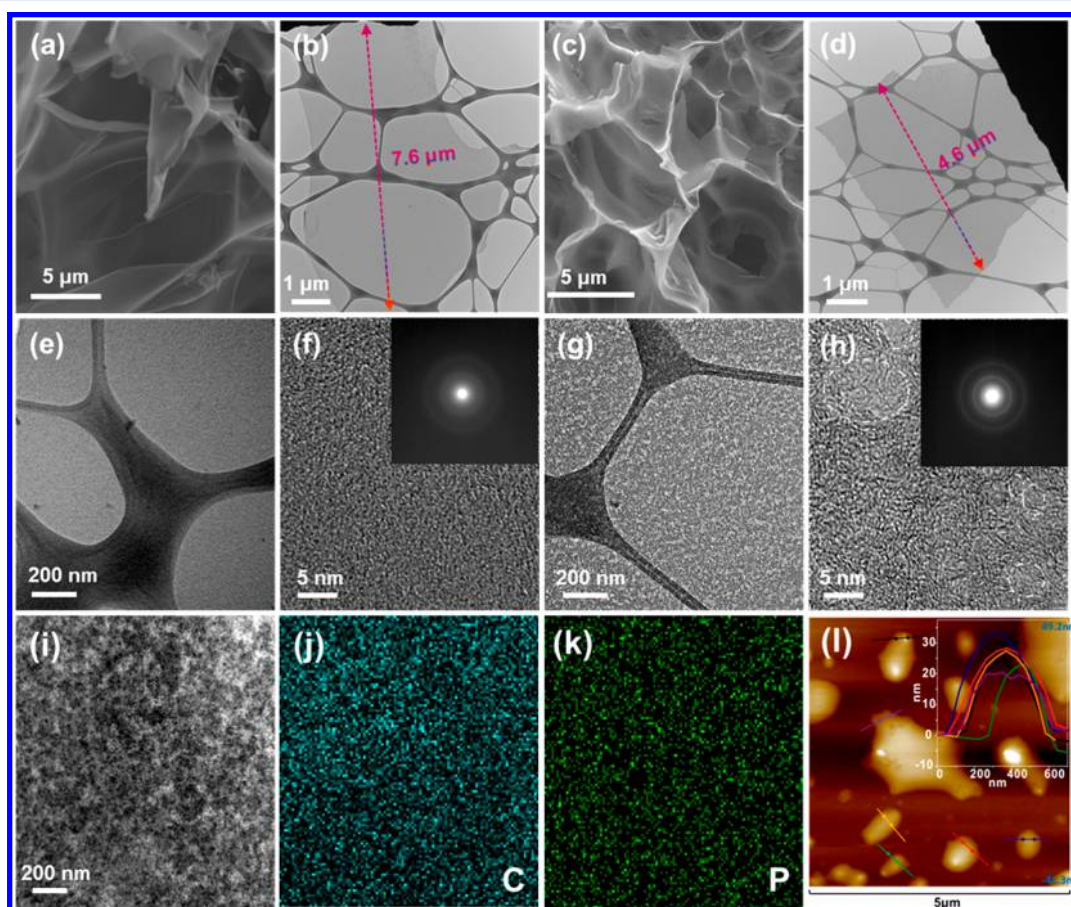
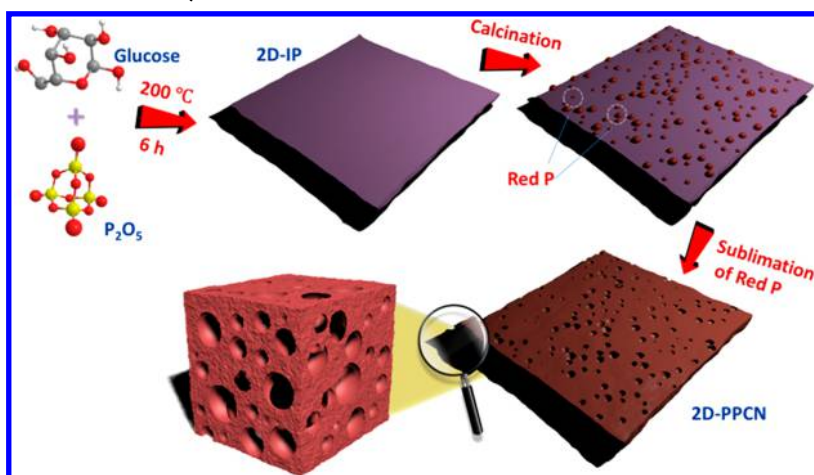


Figure 1. (a, b) SEM and TEM images of 2D-IP. (c, d) SEM and TEM images of 2D-PPCN. (e, f) High-magnification TEM and HRTEM images of 2D-IP. (g, h) High-magnification TEM and HRTEM images of 2D-PPCN. (i) STEM image of 2D-PPCN and its corresponding mapping images (j, k). (l) AFM image (tapping-mode) of 2D-PPCN particles with corresponding height profiles (taken along the dashed line).

oriented morphology and porosity regulation is realized by the multifunctional templating ability of P_2O_5 within the chosen saccharide. During the $200\text{ }^\circ\text{C}$ thermal precarbonization treatment of glucose and P_2O_5 powders in the argon-filled autoclave, P_2O_5 despoils H_2O from glucose to form $\text{H}(\text{HPO}_3)_n\text{OH}$ ($n = 1, 2, 3$, Figure S1–3), followed by transformations to pyrophosphoric acid and glassy, lumpy-like polyphosphoric acid.¹⁶ The subsequent interaction between the long-chain polyphosphoric acids and the remaining P_2O_5 leads

to increased viscosities and a transformation of polyphosphoric acid from oily or wax-like to glassy sheet-like (metaphosphoric acid), which serves as the template for molding of the precarbonized product into a 2D morphology.¹⁸ The obtained product from this stage (Figure S4) is termed the precarbonized 2D intermediate product (2D-IP). During the ensuing calcination at $450\text{ }^\circ\text{C}$, the H_3PO_4 -derived phosphates act as both a source for phosphorus doping and an activation agent for micropore formation within the carbon skeleton.

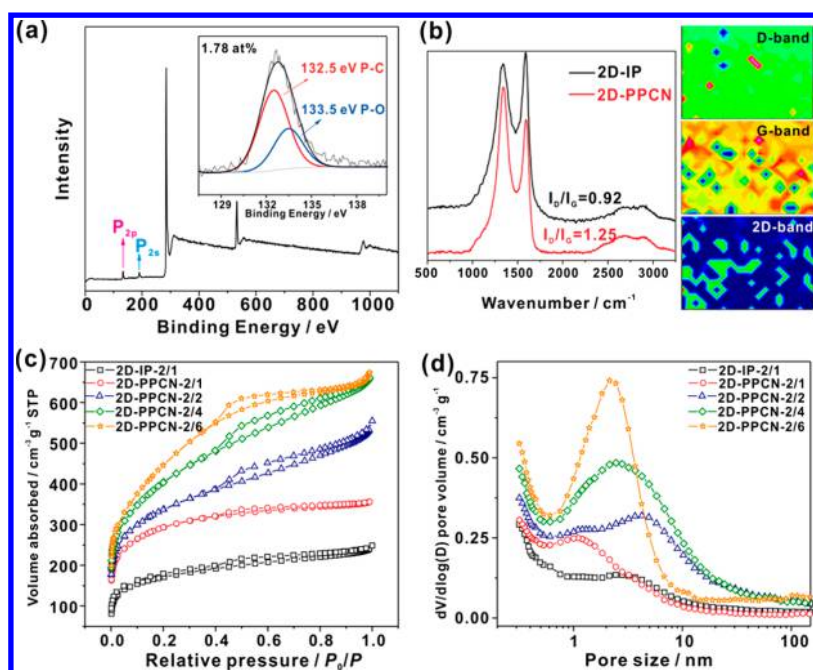


Figure 2. (a) XPS survey scan and P 2p fine spectrum of 2D-PPCN. (b) Comparison of Raman spectra of the precursor and 2D-PPCN. The right side shows the large-area Raman mapping of 2D-PPCN. (c) Nitrogen adsorption–desorption isotherms and (d) pore-size distribution of the synthesized 2D-PPCNs with different weight ratios of glucose and P_2O_5 .

Finally, upon increasing the temperature to 900 °C, the residual P_2O_5 is reduced by carbon to produce nanoscaled red phosphorus.¹⁹ The red phosphorus sublimates during continued calcination, serving as the self-sacrificing template to generate a mesoporous structure within the final product 2D-PPCN.

The obtained 2D-PPCN exhibits well-defined two-dimensionality with a large diameter to thickness ratio, which ensures efficient electron and mass transfer for fast electrochemical kinetics. The adjustment of P_2O_5 content in the raw materials enables a tunable allocation of its contribution in each pore-forming stage, thus allowing precise control of the ratio of micropores to mesopores within a considerable range. The high porosity offers enriched active interfaces, while the porosity tunability considerably expands the applicability of the as-developed 2D-PPCN to accommodate specific electrochemical applications. Additionally, the interaction between the template and the carbon precursor introduces phosphorus heteroatom doping into the carbon lattice, which endows the obtained 2D-PPCN with enhanced surface polarity and enriched potential active sites for certain electrochemical reactions.

3.2. Morphology Analysis. Figure 1 shows the 2D morphology of the as-prepared 2D-IP and 2D-PPCN with a controlled glucose to P_2O_5 weight ratio of 2:1. Figure 1a, b show typical SEM and TEM images of the 2D-IP obtained by the precarbonization process. It can be clearly seen that micrometer-scaled 2D carbon nanosheet assemblies have been formed. The 2D morphology of 2D-IP is oriented by the polymerized product from the in situ-formed H_3PO_4 and P_2O_5 , which is supported by the sheet-like morphology obtained from commercial H_3PO_4 and P_2O_5 treated under the same condition (Figure S5). After high-temperature calcination, the obtained 2D-PPCN inherited the 2D morphology from 2D-IP, showing an interconnected carbon framework consisting of microscale carbon thin sheets (Figure 1c, d). Notably, 2D-PPCN reveals a significant porosity enhancement (Figure 1g, h) in comparison

to 2D-IP (Figure 1e), which is evidenced by the observation of uniformly distributed micro-/mesopores. The FFT patterns in Figure 1f, h reveal the amorphous structure for both 2D-IP and 2D-PPCN, which is also confirmed by their corresponding XRD patterns with a broad peak at ca. 25° (Figure S6). Moreover, the P_2O_5 -assisted cleavage of the C–C bond during the calcination contributed to heteroatomic phosphorus doping in the carbon skeleton, which is confirmed by the uniform elemental distribution in the EELS mapping of 2D-PPCN (Figure 1i–k). Figure 1l displays a typical atomic force microscopy (AFM) image of the obtained 2D-PPCN on a mica surface, where the height profiles reveal the thickness of the nanosheet to be in the range of 20–35 nm. This is consistent with the values determined by means of EELS thickness mapping applied to numerous sites (Figure S7).

3.3. Structure and Composition Properties. X-ray photoelectron spectroscopy (XPS) was carried out to investigate the chemical states within 2D-PPCN (Figure 2a). The survey XPS spectrum clearly shows the P 2s and P 2p peak at approximately 191.0 and 133.0 eV, respectively. The deconvoluted peaks located at 132.5 and 133.5 eV in the P 2p spectra are attributed to P–C bonding and P–O bonding, respectively. This result further manifested that phosphorus atoms were successfully incorporated into the 2D carbon nanosheets during the heat treatment process.²⁰ The P doping content in 2D-PPCN is detected as 1.78 at%. The introduction of P induces structural defects into the carbon matrix and increases the electron delocalization due to the good electron donating properties of P, which endows 2D-PPCN with enriched active sites and improved conductivity and charge transfer.²¹ The carbon structural variation induced by phosphorus doping was also investigated by Raman spectroscopy. As shown in Figure 2b, both 2D-IP and 2D-PPCN exhibit three conspicuous peaks, corresponding to the D band (1335 cm^{-1}), G band (1585 cm^{-1}), and 2D peak (around 2750 cm^{-1} , showing two G' features), respectively. Since the value of I_D/I_G

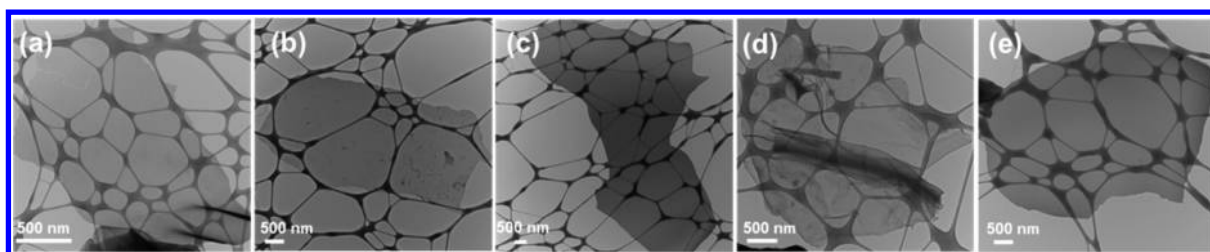


Figure 3. TEM images of 2D-PPCN prepared from different saccharides (a: fructose; b: sucrose; c: starch; d: cellulose; and e: agar).

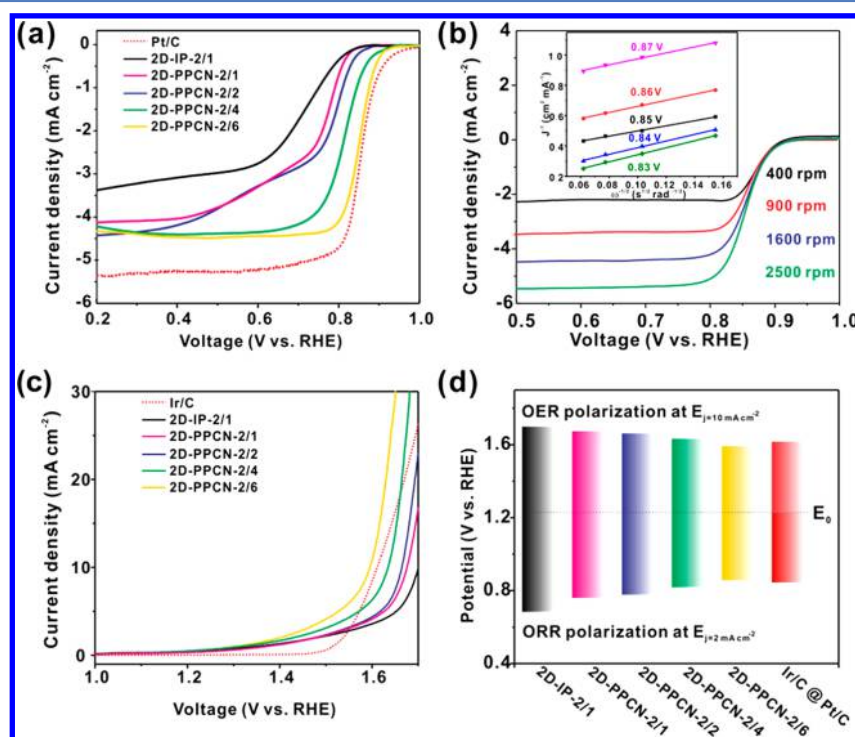


Figure 4. (a) ORR activity at 1600 rpm of the prepared samples compared with 28.8 wt % Pt/C benchmark in 0.1 M KOH at a scan rate of 10 mV s⁻¹. (b) ORR polarization curves of 2D-PPCN-2/6 at various rotating speeds from 400 to 2500 rpm. The inset shows the corresponding K-L plots. (c) OER activity at 1600 rpm of the prepared samples compared with 20 wt % Ir/C. (d) Potential differences between the $E_{j=2}$ of ORR and $E_{j=10}$ of OER for all the catalysts.

semiquantitatively reflects the amount of structural defects, the significantly higher I_D/I_G value of 1.25 for 2D-PPCN than that of 2D-IP ($I_D/I_G = 0.92$) indicates the considerable enhancement of structural defects after phosphorus doping.

As aforementioned, the micropore and mesopore formations are performed by different templating mechanisms in separate reaction stages. Therefore, regulating the P_2O_5 content in the precursor allows for controlled allocation of the template's contributions to each pore-forming stage, such that the relative abundances of micropores and mesopores in 2D-PPCN can be easily adjusted. Specifically, when conducting 2D-PPCN synthesis with varied glucose to P_2O_5 weight ratios (denoted as 2D-PPCN-2/1 to 2/6, as indicated in the [Experimental Section](#)), the content of micropores formed in the first calcination stage at 450 °C is fixed due to the constant glucose content and excess of P_2O_5 among all these specimens. The previously formed phosphoric acid and derived phosphates in the precarbonization process etch the carbon substrate to yield micropores in this calcination stage.²² Subsequently, at an elevated temperature of 900 °C, the residual P_2O_5 is reduced by carbon and forms nanoscale red phosphorus, which sublimates during continued calcination and leaves an abundance of

mesopores in the product carbon sheets. It is noteworthy that in this high-temperature pore-forming stage, the excessive P_2O_5 corrosion causes collapse and consumption of the microporous substrate, which ultimately leads to reduced microporosity at the expense of increased mesoporosity. Benefiting from this differential variation tendency, the micropore and mesopore contents in 2D-PPCNs can be well regulated through the rational distribution of P_2O_5 in different pore-forming stages. As a proof-of-concept, BET measurements were performed to investigate the porosity variation among the 2D-PPCNs with varied precursor constitution. The N_2 adsorption/desorption isotherms show combined II/IV type curves with strong adsorption at medium and low relative pressure, indicating the coexistence of microporous and mesoporous structures in each 2D-PPCN. A significant porosity enhancement was obtained when 2D-IP was converted into 2D-PPCN through the high-temperature calcination. As the glucose to P_2O_5 weight ratio varied from 2:1 to 2:6 in the precursor, a continuously strengthened N_2 adsorption/desorption behavior was observed in the range of $P/P_0 = 0.5–0.8$ (Figure 2c), indicating the increase of mesoporosity. This result was confirmed by the successive increase of mesopores in the pore size distribution

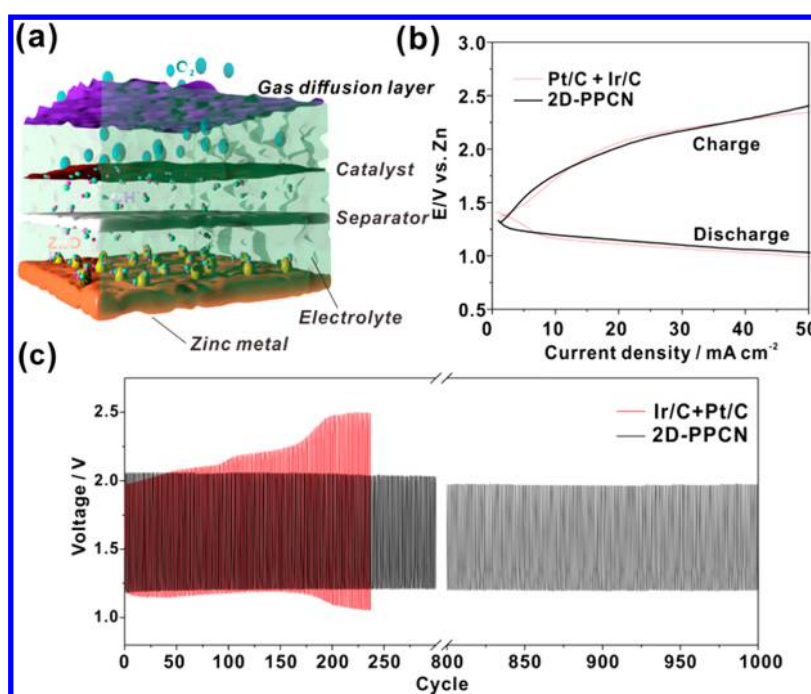


Figure 5. (a) Schematic illustration of the zinc air battery configuration. (b) Galvanodynamic charge/discharge polarization curves of 2D-PPCN and Pt/C+Ir/C based air electrode. (c) Galvanostatic charge/discharge curves of 2D-PPCN based zinc air battery at a current density of 10 mA cm^{-2} with each cycle being 10 min.

(Figure 2d), as well as the variation of porous morphologies of 2D-PPCNs by TEM observation (Figure S8, S9). Detailed pore structure characteristics of 2D-PPCNs with varying glucose to P_2O_5 ratios are summarized in Table S1. Notably, both the specific surface area (SSA) and pore volume contributed by micropores ($S_{\text{BET}(\text{micro})}$ and V_{micro}) in 2D-PPCNs continuously decrease in correlation with the increase of P_2O_5 in the precursor, while those of mesopores exhibit a successive enhancement (Figure S10). Thus, the relative ratio of micropores to mesopores (represented by $S_{\text{BET}(\text{micro})}/S_{\text{BET}(\text{meso})}$ and $V_{\text{micro}}/V_{\text{meso}}$) consistently declines as the P_2O_5 weight increases in the precursor. Moreover, steady enhancements of the total surface area (S_{BET}) and pore volume (V_{total}) were achieved by increasing P_2O_5 usage, reaching their highest values of $1555.8 \text{ m}^2 \text{ g}^{-1}$ and $1.383 \text{ cm}^3 \text{ g}^{-1}$, respectively, at a glucose to P_2O_5 weight ratio of 2:6. Since the increase in SSA and pore volume becomes slow because of the limited utilization of P_2O_5 , thus glucose/ $\text{P}_2\text{O}_5 = 2:6$ is set as the maximum ratio. These results demonstrate the high porosity and great porosity tunability of 2D-PPCN, which suggests that it has a high potential for meeting the variable requirements of different electrochemical applications.²³

Considering the success of 2D-PPCN synthesis from glucose, an extended selection of saccharide carbon sources including fructose, sucrose, starch, cellulose, and agar were investigated for 2D-PPCN production. Excellent 2D morphological and structural consistency was observed for all these saccharides, as shown in Figure 3 (TEM) and Figure S11–S13 (SEM, XPS, and Raman). These results indicate the universality of this strategy toward 2D-PPCN production, which could be important for controlling the cost of potential large-scale manufacturing.

3.4. Electrochemical Properties of 2D-PPCN. In view of the unique structural features and functions of 2D-PPCN, the prepared samples (with different glucose/ P_2O_5 mass ratios)

were employed as bifunctional oxygen catalysts. In this work, there is no great difference of P doping contents within the synthesized samples when varying the glucose/ P_2O_5 ratio; which was proved by the full XPS spectrum as shown in Figure S14. The specific surface area, pore size distribution, and surface functionalities are regarded as the most significant features of carbon materials for electrocatalytic performance in applications such as Li– O_2 batteries or Zinc-air batteries.²⁴ However, relatively little attention has been paid to the structural effects of carbon materials on their electrochemical behavior in these batteries. To gain insights into the activity difference among catalysts with different porous structures, it is desirable to synthesize catalysts with similar morphologies from one single precursor or template.

The bifunctional oxygen electrocatalytic performances of 2D-PPCNs were tested in 0.1 M KOH using a standard three-electrode system, with potentials reported versus a reversible hydrogen electrode (RHE). For comparison, commercial Pt/C (28.8 wt %) and Ir/C (20 wt %) were measured as the ORR and OER benchmarks, respectively. Regarding the ORR curves (Figure 4a), the half wave potential of 2D-PPCN-2/6 is 0.85 V, which is the same as that of Pt/C (0.85 V) and much higher than that of 2D-IP-2/1 (0.70 V), 2D-PPCN-2/1 (0.76 V), 2D-PPCN-2/2 (0.77 V), and 2D-PPCN-2/4 (0.82 V). For a further investigation on the reaction mechanism, LSV curves of different rotation speeds (400, 900, 1600, and 2500 rpm) were also conducted, as shown in Figure 4b. The number of electrons transferred (n) was calculated to be ~ 3.6 at 0.83–0.87 V from the slopes of the Koutecky–Levich plots, indicating the nearly complete reduction of O_2 to H_2O on the surface of the 2D-PPCN-2/6.^{25,26} Moreover, 2D-PPCN-2/6 presents a more positive onset potential (E_{onset} defined as the potential at 0.1 mA cm^{-2}) of 0.92 V and half-wave potential ($E_{1/2}$) of 0.85 V than those of Pt/C (0.96 and 0.85 V, respectively). A comparable limiting current density (J_L) as high as 4.5 mA

cm^{-2} was also delivered by 2D-PPCN-2/6. To facilitate faster mass transport, a larger pore size and shorter diffusion pathway would be preferred, but such structures often possess limited surface area and cannot supply numerous accessible active-sites for ORR.^{14b} The catalytic activity of carbon based electrocatalysts is improved by a surface atomistic structure that is well-suited to the physical and electrochemical properties of the redox reactions. In general, a structure possessing a high surface area often has a small pore size, which is inconvenient for efficient mass transport. From this point of view, a hierarchical structure with abundant mesopores is rational for achieving a high effective surface area without compromising mass transport. High concentrations of P dopants and exposed active sites in combination with optimized porosity are the main reason for the high-efficiency ORR process in this case.²⁷ In the case of the OER activity (Figure 4c), an overpotential of 365 mV was measured for 2D-PPCN-2/6 after IR-correction at a current density of 10 mA cm^{-2} , outperforming those of 2D-IP-2/1 (470 mV), 2D-PPCN-2/1 (445 mV), 2D-PPCN-2/2 (434 mV), and 2D-PPCN-2/4 (404 mV). The OER kinetic of 2D-PPCN-2/6 is even superior to Ir/C (381 mV). The fastest OER electrocatalytic performance of 2D-PPCN-2/6 is further confirmed by its smaller Tafel slope relative to the other samples (Figure S16). Therefore, the best bifunctional activity is demonstrated by 2D-PPCN-2/6 (Figure 4d), which has the lowest overpotential difference of 0.74 V defined by the difference between 2 mA cm^{-2} for ORR and 10 mA cm^{-2} for OER. The superior electrochemical performances of 2D-PPCN-2/6 lie in the better utilization of doping sites and promotion of mass transport since most of the catalytic sites are located at the surface of the interconnected porous structure. The highly expanded electrode/electrolyte interface provides more active sites and allows for the rapid release of O_2 during the catalytic process, facilitating the electrocatalytic process.

Zn-air batteries represent an attractive option to increase the range and lower the cost of electric vehicles, due to their high specific energy and lower cost relative to Li-ion batteries.²⁸ For rechargeable Zn-air batteries, the bifunctional air electrode catalyst should exhibit minimal ORR/OER overpotentials and high cyclic durability.²⁹ Based on the operating mechanism of Zn-air batteries, an interconnected open-pore system with high SSA for the catalyst is conducive to electrolyte immersion, Zn^{2+} diffusion, and storage of the solid-state discharge product (ZnO).³⁰ A robust pore structure can provide a convenient pathway for O_2 diffusion during charging and discharging, while high-aspect-ratio particles enable efficient electron transfer along their long axes. 2D porous carbon materials, due to their robust pore structure and nanoscale thickness versus microscale lateral dimension, are thus a strong candidate for bifunctional air electrodes.

Full-cell Zn-air battery tests in an atmospheric air environment (illustration as shown in Figure 5a) were conducted to reveal the rechargeability and stability of 2D-PPCN-2/6 within the air electrode. As discerned in Figure 5b, similar open circuit voltage (about 1.40 V) and charge–discharge galvanodynamic performance were obtained by 2D-PPCN in comparison to the benchmark mixture of Pt/C and Ir/C. Regarding the cycling performance of Zn-air batteries at a current density of 10 mA cm^{-2} , the 2D-PPCN based battery displays highly superior durability to that of Pt/C+Ir/C (Figure 5c). Specifically, the commercial Pt/C+Ir/C based air electrode demonstrates less than 250 cycles before showing excessive overpotentials. In contrast, 2D-PPCN displays a significantly long cycle-life of

over 1000 cycles with decreasing overpotentials, measured by the voltage gap between discharge and charge potentials. Upon 1000 cycles, the overpotential of 2D-PPCN reduced from 0.87 to 0.78 V. The impressive performance of 2D-PPCN is proposed to result from its unique architecture, as alluded to earlier. The phosphorus doping into carbon materials could reduce the charge polarization, which stems from the difference in electronegativity relative to nondoped carbon.³¹ Moreover, the 2D structure with porosity and interconnectivity can supply additional space available for ion and oxygen transportation, while maintaining sufficient conductivity for solid-state electronic transfer, thus giving rise to low diffusion polarization losses and long cycling stability.

4. CONCLUSION

In summary, large-size two-dimensional porous carbon nano-sheets were harvested through flexible multifunctional templating of saccharides by P_2O_5 . The obtained 2D-PPCN exhibits a 20–35-nm-thick 2D morphology, considerable heteroatomic P-doping, and excellent porosity tunability. These unique features endow 2D-PPCN with fast mass and electron transfer, thus making it attractive for electrochemical applications. The highest performing 2D-PPCN-2/6 based catalyst shows well-balanced catalytic activity for both the ORR and OER, which is comparable to that of commercial Pt/C and Ir/C counterparts in half-cell testing. The practicality of the material is further highlighted by an excellent stability in a rechargeable zinc–air battery air electrode utilizing atmospheric oxygen. The findings in this work offer a new strategy for efficient production of advanced 2D carbon, which could have potential for other energy storage and conversion technologies such as hydrogen storage, sensors, supercapacitors, and other batteries.

■ ASSOCIATED CONTENT

📄 Supporting Information

The Supporting Information is available free of charge on the ACS Publications website at DOI: 10.1021/acscatal.7b02739.

Digital photographs of the samples before and after solid-state hydrothermal treatment, structural evolution of the dehydration process of glucose, structural evolution of P_4O_{10} to chain molecules of $\text{H}(\text{HPO}_3)_4\text{OH}$, SEM and TEM images, XRD pattern, STEM images and EELS spectra, Raman and XPS spectra, OPR polarization curves, Tafel plots, and porous structure parameters (PDF)

■ AUTHOR INFORMATION

Corresponding Authors

*E-mail: wangdl81125@hust.edu.cn.

*E-mail: zhwchen@uwaterloo.ca.

ORCID

Wen Lei: 0000-0003-3069-5299

Zachary P. Cano: 0000-0002-2433-297X

Xiaolei Wang: 0000-0002-7751-4849

Deli Wang: 0000-0003-2023-6478

Zhongwei Chen: 0000-0003-3463-5509

Notes

The authors declare no competing financial interest.

ACKNOWLEDGMENTS

This work was supported by the National Natural Science Foundation (21573083), 1000 Young Talent (to Deli Wang). The authors also wish to acknowledge the support provided by the Natural Sciences and Engineering Research Council of Canada (NSERC) and by the University of Waterloo and the Waterloo Institute for Nanotechnology. We acknowledge the support of the China Scholarship Council (CSC).

REFERENCES

(1) (a) Novoselov, K. S.; Geim, A. K.; Morozov, S. V.; Jiang, D.; Zhang, Y.; Dubonos, S. V.; Grigorieva, I. V.; Firsov, A. A. Electric Field Effect in Atomically Thin Carbon Films. *Science* **2004**, *306*, 666–669. (b) Brownson, D. A. C.; Kampouris, D. K.; Banks, C. E. An Overview of Graphene in Energy Production and Storage Applications. *J. Power Sources* **2011**, *196*, 4873–4885.

(2) Kalantar-zadeh, K.; Ou, J. Z.; Daeneke, T.; Mitchell, A.; Sasaki, T.; Fuhrer, M. S. Two Dimensional and Layered Transition Metal Oxides. *Appl. Mater. Today* **2016**, *5*, 73–89.

(3) Chhowalla, M.; Shin, H. S.; Eda, G.; Li, L. J.; Loh, K. P.; Zhang, H. The Chemistry of Two-Dimensional Layered Transition Metal Dichalcogenide Nanosheets. *Nat. Chem.* **2013**, *5*, 263–275.

(4) Lukatskaya, M.; Mashtalir, O.; Ren, C.; Dall'Agnesse, Y.; Rozier, P.; Taberna, P.; Naguib, M.; Simon, P.; Barsoum, M.; Gogotsi, Y. Cation Intercalation and High Volumetric Capacitance of Two-Dimensional Titanium Carbide. *Science* **2013**, *341*, 1502–1505.

(5) Fan, X.; Yu, C.; Yang, J.; Ling, Z.; Hu, C.; Zhang, M.; Qiu, J. A Layered-Nanospace-Confinement Strategy for the Synthesis of Two-Dimensional Porous Carbon Nanosheets for High-Rate Performance Supercapacitors. *Adv. Energy Mater.* **2015**, *5*, 1401761.

(6) Lee, K.; Kim, S. W.; Toda, Y.; Matsuishi, S.; Hosono, H. Dicalcium Nitride as a Two-Dimensional Electride with An Anionic Electron Layer. *Nature* **2013**, *494*, 336–340.

(7) Tao, L.; Cinquanta, E.; Chiappe, D.; Grazianetti, C.; Fanciulli, M.; Dubey, M.; Molle, A.; Akinwande, D. Silicene Field-Effect Transistors Operating at Room Temperature. *Nat. Nanotechnol.* **2015**, *10*, 227–231.

(8) Pei, J.; Gai, X.; Yang, J.; Wang, X.; Yu, Z.; Choi, D. Y.; Luther-Davies, B.; Lu, Y. Producing Air-Stable Monolayers of Phosphorene and Their Defect Engineering. *Nat. Commun.* **2016**, *7*, 10450.

(9) Zhang, J.; Chen, Y.; Wang, X. Two-Dimensional Covalent Carbon Nitride Nanosheets: Synthesis, Functionalization, and Applications. *Energy Environ. Sci.* **2015**, *8*, 3092–3108.

(10) Bhimanapati, G. R.; Lin, Z.; Meunier, V.; Jung, Y.; Cha, J.; Das, S.; Xiao, D.; Son, Y.; Strano, M. S.; Cooper, V. R.; Liang, L.; Louie, S. G.; Ringe, E.; Zhou, W.; Kim, S. S.; Naik, R. R.; Sumpter, B. G.; Terrones, H.; Xia, F.; Wang, Y.; Zhu, J.; Akinwande, D.; Alem, N.; Schuller, J. A.; Schaak, R. E.; Terrones, M.; Robinson, J. A. Recent Advances in Two-Dimensional Materials beyond Graphene. *ACS Nano* **2015**, *9*, 11509–11539.

(11) (a) Liu, J.; Liu, X. W. *Adv. Mater.* **2012**, *24*, 4097–4111. (b) Fan, H.; Shen, W. Carbon Nanosheets: Synthesis and Application. *ChemSusChem* **2015**, *8*, 2004–2027.

(12) (a) Higgins, D.; Zamani, P.; Yu, A.; Chen, Z. The Application of Graphene and Its Composites in Oxygen Reduction Electrocatalysis: A Perspective and Review of Recent Progress. *Energy Environ. Sci.* **2016**, *9*, 357–390. (b) Yang, D.-S.; Bhattacharjya, D.; Song, M. Y.; Yu, J.-S. Highly Efficient Metal-Free Phosphorus-Doped Platelet Ordered Mesoporous Carbon for Electrocatalytic Oxygen Reduction. *Carbon* **2014**, *67*, 736–743.

(13) (a) Du, Q. S.; Tang, P. D.; Huang, H. L.; Du, F. L.; Huang, K.; Xie, N. Z.; Long, S. Y.; Li, Y. M.; Qiu, J. S.; Huang, R. B. A New Type of Two-Dimensional Carbon Crystal Prepared from 1,3,5-Trihydroxybenzene. *Sci. Rep.* **2017**, *7*, 40796. (b) Yuan, K.; Hu, T.; Xu, Y.; Graf, R.; Shi, L.; Forster, M.; Pichler, T.; Riedl, T.; Chen, Y.; Scherf, U. Nitrogen-Doped Porous Carbon/Graphene Nanosheets Derived from Two-Dimensional Conjugated Microporous Polymer Sandwiches with

Promising Capacitive Performance. *Mater. Chem. Front.* **2017**, *1*, 278–285.

(14) (a) Song, S.; Liang, Y.; Li, Z.; Wang, Y.; Fu, R.; Wu, D.; Tsiakaras, P. Effect of Pore Morphology of Mesoporous Carbons on the Electrocatalytic Activity of Pt Nanoparticles for Fuel Cell Reactions. *Appl. Catal., B* **2010**, *98*, 132–137. (b) Wu, R.; Chen, S.; Zhang, Y.; Wang, Y.; Nie, Y.; Ding, W.; Qi, X.; Wei, Z. Controlled Synthesis of Hollow Micro/Meso-Pore Nitrogen-Doped Carbon with Tunable Wall Thickness and Specific Surface Area as Efficient Electrocatalysts for Oxygen Reduction Reaction. *J. Mater. Chem. A* **2016**, *4*, 2433–2437. (c) Lee, S.; Choun, M.; Ye, Y.; Lee, J.; Mun, Y.; Kang, E.; Hwang, J.; Lee, Y. H.; Shin, C. H.; Moon, S. H.; Kim, S. K.; Lee, E.; Lee, J. Designing a Highly Active Metal-Free Oxygen Reduction Catalyst in Membrane Electrode Assemblies for Alkaline Fuel Cells: Effects of Pore Size and Doping-Site Position. *Angew. Chem., Int. Ed.* **2015**, *54*, 9230–9234.

(15) (a) Tang, J.; Liu, J.; Li, C.; Li, Y.; Tade, M. O.; Dai, S.; Yamauchi, Y. Synthesis of nitrogen-doped mesoporous carbon spheres with extra-large pores through assembly of diblock copolymer micelles. *Angew. Chem., Int. Ed.* **2015**, *54*, 588–593. (b) Zheng, S. S.; Li, X. R.; Yan, B. Y.; Hu, Q.; Xu, Y. X.; Xiao, X.; Xue, H. G.; Pang, H. Transition-Metal (Fe, Co, Ni) Based Metal-Organic Frameworks for Electrochemical Energy Storage. *Adv. Energy Mater.* **2017**, *7*, 1602733.

(16) (a) Zhuang, X. D.; Zhang, F.; Wu, D. Q.; Feng, X. L. Graphene Coupled Schiff-base Porous Polymers: Towards Nitrogen-enriched Porous Carbon Nanosheets with Ultrahigh Electrochemical Capacity. *Adv. Mater.* **2014**, *26*, 3081–3086. (b) Wei, W.; Liang, H. W.; Parvez, K.; Zhuang, X. D.; Feng, X. L.; Müllen, K. Nitrogen-Doped Carbon Nanosheets with Size-Defined Mesopores as Highly Efficient Metal-Free Catalyst for the Oxygen Reduction Reaction. *Angew. Chem.* **2014**, *126*, 1596–1600.

(17) Scott, R. W.; Moore, W. E.; Effland, M. J.; Millett, M. A. Ultraviolet Spectrophotometric Determination of Hexoses, Pentoses, and Uronic Acids after Their Reactions with Concentrated Sulfuric Acid. *Anal. Biochem.* **1967**, *21*, 68–80.

(18) Corbridge, D.E.C. *Phosphorus Chemistry Biochemistry and Technology*, 6th ed.; 2013; p 188.

(19) Xiang, B.; Wang, P.; Zhang, X.; Dayeh, S. A.; Aplin, D. P.; Soci, C.; Yu, D.; Wang, D. Rational Synthesis of P-Type Zinc Oxide Nanowire Arrays Using Simple Chemical Vapor Deposition. *Nano Lett.* **2007**, *7*, 323–328.

(20) (a) Puziy, A. M.; Poddubnaya, O. I.; Socha, R. P.; Gurgul, J.; Wisniewski, M. XPS and NMR Studies of Phosphoric Acid Activated Carbons. *Carbon* **2008**, *46*, 2113–2123. (b) Yang, D. S.; Bhattacharjya, D.; Inamdar, S.; Park, J.; Yu, J. S. Phosphorus-Doped Ordered Mesoporous Carbons with Different Lengths as Efficient Metal-Free Electrocatalysts for Oxygen Reduction Reaction in Alkaline Media. *J. Am. Chem. Soc.* **2012**, *134*, 16127–16130.

(21) Ma, T. Y.; Ran, J.; Dai, S.; Jaroniec, M.; Qiao, S. Z. Phosphorus-Doped Graphitic Carbon Nitrides Grown in Situ on Carbon-Fiber Paper: Flexible and Reversible Oxygen Electrodes. *Angew. Chem., Int. Ed.* **2015**, *54*, 4646–4650.

(22) Teng, H.; Yeh, T.; Hsu, L. Preparation of Activated Carbon from Bituminous Coal with Phosphoric Acid Activation. *Carbon* **1998**, *36*, 1387–1395.

(23) (a) Paraknowitsch, J. P.; Thomas, A. Doping Carbons beyond Nitrogen: An Overview of Advanced Heteroatom Doped Carbons with Boron, Sulphur and Phosphorus for Energy Applications. *Energy Environ. Sci.* **2013**, *6*, 2839–2855. (b) Hou, H.; Shao, L.; Zhang, Y.; Zou, G.; Chen, J.; Ji, X. Large-Area Carbon Nanosheets Doped with Phosphorus: A High-Performance Anode Material for Sodium-Ion Batteries. *Adv. Sci.* **2017**, *4*, 1600243.

(24) Liang, J.; Zheng, Y.; Chen, J.; Liu, J.; Hulicova-Jurcakova, D.; Jaroniec, M.; Qiao, S. Z. Facile Oxygen Reduction on A Three-Dimensionally Ordered Macroporous Graphitic C₃N₄/Carbon Composite Electrocatalyst. *Angew. Chem., Int. Ed.* **2012**, *51*, 3892–3896.

(25) (a) Gong, K.; Du, F.; Xia, Z.; Durstock, M.; Dai, L. Nitrogen-Doped Carbon Nanotube Arrays with High Electrocatalytic Activity for Oxygen Reduction. *Science* **2009**, *323*, 760–763. (b) Zhang, M.;

Yan, Y.; Gong, K.; Mao, L.; Guo, Z.; Chen, Y. Electrostatic Layer-by-Layer Assembled Carbon Nanotube Multilayer Film and Its Electrocatalytic Activity for O₂ Reduction. *Langmuir* **2004**, *20*, 8781–8785.

(26) Fu, X.; Zamani, P.; Choi, J. Y.; Hassan, F. M.; Jiang, G.; Higgins, D. C.; Zhang, Y.; Hoque, M. A.; Chen, Z. In Situ Polymer Graphenization Ingrained with Nanoporosity in a Nitrogenous Electrocatalyst Boosting the Performance of Polymer-Electrolyte-Membrane Fuel Cells. *Adv. Mater.* **2017**, *29*, 1604456.

(27) Liu, Z. W.; Peng, F.; Wang, H. J.; Yu, H.; Zheng, W. X.; Yang, J. Phosphorus-Doped Graphite Layers with High Electrocatalytic Activity for the O₂ Reduction in an Alkaline Medium. *Angew. Chem., Int. Ed.* **2011**, *50*, 3257–3261.

(28) Li, Y.; Dai, H. Recent Advances in Zinc–Air Batteries. *Chem. Soc. Rev.* **2014**, *43*, 5257–5275.

(29) (a) Fu, J.; Cano, Z. P.; Park, M. G.; Yu, A.; Fowler, M.; Chen, Z. Electrically Rechargeable Zinc–Air Batteries: Progress, Challenges, and Perspectives. *Adv. Mater.* **2017**, *29*, 1604685. (b) Gu, P.; Zheng, M. B.; Zhao, Q. X.; Xiao, X.; Xue, H. G.; Pang, H. Rechargeable Zinc–Air Batteries: A Promising Way to Green Energy. *J. Mater. Chem. A* **2017**, *5*, 7651–7666.

(30) Cao, R.; Lee, J.-S.; Liu, M.; Cho, J. Recent Progress in Non-Precious Catalysts for Metal-Air Batteries. *Adv. Energy Mater.* **2012**, *2*, 816–829.

(31) Zhang, C.; Mahmood, N.; Yin, H.; Liu, F.; Hou, Y. Synthesis of Phosphorus-Doped Graphene and Its Multifunctional Applications for Oxygen Reduction Reaction and Lithium Ion Batteries. *Adv. Mater.* **2013**, *25*, 4932–4937.